

# ViSymRe: Vision-guided Multimodal Symbolic Regression

Da Li<sup>a</sup>, Junping Yin<sup>c,d,f</sup>, Jin Xu<sup>c</sup>, Xinxin Li<sup>e</sup>, Juan Zhang<sup>b,\*</sup>

<sup>a</sup>Academy for Advanced Interdisciplinary Studies, Northeast Normal University, Changchun, 130024, Jilin, China

<sup>b</sup>Institute of Artificial Intelligence, Beihang University, Beijing, 100191, Beijing, China

<sup>c</sup>Institute of Applied Physics and Computational Mathematics, Beijing, 100094, Beijing, China

<sup>d</sup>National Key Laboratory of Computational Physics, Beijing, 100088, Beijing, China

<sup>e</sup>School of Mathematical Sciences, East China Normal University, Shanghai, 200241, Shanghai, China

<sup>f</sup>Shanghai Zhangjiang Institute of Mathematics, Shanghai, 201203, Shanghai, China

---

## Abstract

Extracting simple mathematical expression from an observational dataset to describe complex natural phenomena is one of the core objectives of artificial intelligence (AI). This field is known as symbolic regression (SR). Traditional SR models are based on genetic programming (GP) or reinforcement learning (RL), facing well-known challenges, such as low efficiency and overfitting. Recent studies have integrated SR with large language models (LLMs), enabling fast zero-shot inference by learning mappings from millions of dataset-expression pairs. However, since the input and output are inherently different modalities, such models often struggle to converge effectively. In this paper, we introduce **ViSymRe**, a vision-guided multimodal SR model that incorporates the third resource—expression graph—to bridge the modality gap. Different from traditional multimodal models, ViSymRe is trained to extract vision, termed virtual vision, from datasets, without relying on the global availability of expression graphs, which addresses the essential challenge of visual SR, i.e., expression graphs are not available during inference. Evaluation results on multiple mainstream benchmarks show that ViSymRe achieves more competitive performance than the state-of-the-art dataset-only baselines. The expressions predicted by ViSymRe not only fit the dataset well but are also simple and structurally accurate—goals that SR models strive to achieve.

*Keywords:* Vision-guided symbolic regression, Multimodal learning, Virtual vision

---

## 1. Introduction

Revealing the underlying mechanisms and laws of natural phenomena from observational data has emerged as a core goal in contemporary artificial intelligence (AI). In 2009, Schmidt and Lipson published an influential study in *Science*, demonstrating how symbolic regression (SR) can derive laws in classical mechanics, including Hamiltonians, Lagrangians, and other laws of geometric and momentum conservation, from motion-tracking data [1]. This work highlights the potential of SR in facilitating scientific discovery [2, 3]. As a data-driven method, SR aims to automatically discover mathematical expressions that best describe the relationships between variables and target (also known as the dependent variable, output, response, or outcome in different fields) from the input datasets. In fields such as physics, chemistry, and ecology, SR is extensively used [4, 5, 6, 7].

In the early 1990s, Koza introduced genetic programming (GP) for SR, where the individuals are regarded as expression trees with operators, variables, and constants as nodes [8]. GP simulates biological processes like gene replication, crossover, and mutation to evolve individuals [9, 10, 11, 12]. When the initial population is large and the probabilities associated with crossover and mutation are well-calibrated, GP-based models show resistance to local optima. However, they are usually inefficient. The bottleneck lies in the vast search space of expressions and the lack of guidance, which has prompted the development of deep learning (DL)-based SR models that guide expression search

---

\*Corresponding author at: Institute of Artificial Intelligence, Beihang University

*Email addresses:* dli@nenu.edu.cn (Da Li), yinjp829829@126.com (Junping Yin), xujin22@gscaep.ac.cn (Jin Xu), 51265500102@stu.ecnu.edu.cn (Xinxin Li), zhang\_juan@buaa.edu.cn (Juan Zhang)

through gradient descent (GD) or reinforcement learning (RL) [13, 14, 15, 16]. But these models do not fundamentally address the problem of the vast search space, resulting in limited efficiency improvements. In addition, both GP-based and DL-based models train a new model for each problem, limiting their ability to accumulate experience from old problems to solve new problems faster, which is another reason for their inefficiency.

Recent advances in SR have introduced pretrained architectures [17, 18, 19, 20], which learn the mappings between datasets and expressions, similar to large language models (LLMs). Expression prediction can be completed with just a single forward pass, demonstrating higher efficiency compared to GP-based and DL-based models. However, these models overlook a crucial aspect: dataset and expression are two distinct modalities, unlike in machine translation, where both languages belong to the same modality [21]. As a result, existing pretrained SR models cannot achieve the same convergence level as LLMs. To address this issue, we introduce expression graph—a key resource that is readily available but has been overlooked in previous studies.

Currently, vision-guided modeling have proven effective in various machine learning domains. Plausibility is obvious. For example, in the case of machine translation, despite originating from a distinct language, the English word “Dog” and the German word “Hund” share identical underlying visual perception. Multimodal technology has the potential to extend to symbolic regression, allowing the model to analyze typical patterns or shapes presented in the graphs to select suitable base functions, thereby potentially reducing the search space (see in Fig. ‘1). However, existing multimodal models typically rely on specialized equipment such as CT and radar, or precreated databases to ensure that visual modalities are readily available during training and inference, which is challenging for SR. The key obstacle is that traditional 2D visualization is inadequate for high-dimensional datasets, making it difficult to acquire graphs directly.

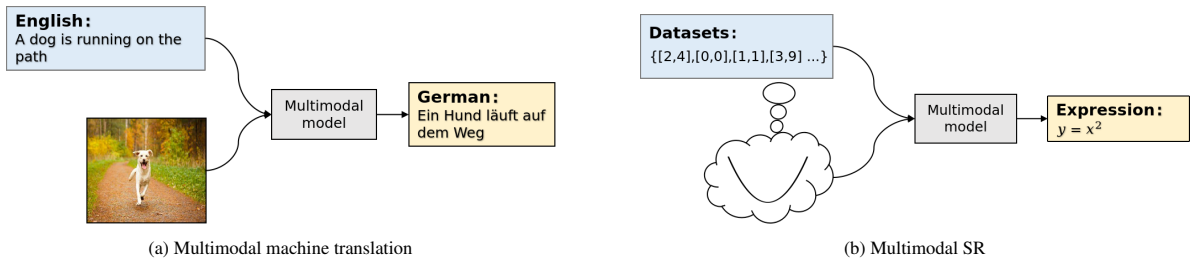


Figure 1: The similar role of vision in machine translation and SR.

To address this issue, we propose a pruning-based method that focuses on visualizing the expressions rather than the datasets. The core idea is to decouple the multivariate expressions into several unrelated univariate expressions, which can be visualized as independent 2D curves and subsequently re-integrated into the high-dimensional space. However, this method relies on the premise that expression structure is known during training, which typically does not hold during inference (only the datasets are available). To bridge this gap, we introduce a novel concept: virtual vision, which is abstracted from datasets by a dedicated neural network module, termed the virtual visual encoder, to replace the real vision extracted from the expression graphs.

Based on this, we present **ViSymRe**. It learns the mapping from the fused representation of expression graphs and datasets to expression skeletons during training to build a robust multimodal SR model and achieves graph-free multimodal inference based on virtual vision. ViSymRe consists of two independent visual processing pipelines: one for real visual encoding and the other for virtual visual encoding, where the former provides supervision for the latter. But the virtual visual encoder does not attempt to directly reconstruct expression graphs or regress the encoded visual features, as doing so often leads to the well-known mean collapse problem, which is primarily attributed to the use of mean squared error (MSE) loss [22]. Therefore, we introduce feature quantization in the real visual encoding process to map the visual features to their nearest codebook vectors in a learnable finite-dimensional codebook space [23]. The virtual visual encoder is trained to predict the indices of the codebook vectors corresponding to the visual features. This is a typical multi-classification problem, thereby allowing stable optimization with cross-entropy loss and naturally avoiding the mean collapse phenomenon. Once the virtual visual features are predicted, multimodal SR inference becomes a matter of course.

Overall, our main innovations are as follows:

- We propose ViSymRe, a vision-guided multimodal SR framework, that introduces expression graphs to bridge the modality gap between datasets and expressions, moving beyond the traditional dataset-only SR paradigm. Extensive experiments show that ViSymRe outperforms state-of-the-art baselines across multiple benchmarks, demonstrating its potential to advance the field of SR.
- We introduce virtual vision, which is abstracted from the datasets to substitute for the real vision extracted by expression graphs, enabling ViSymRe to generalize its multimodal capability to graph-free scenarios, thereby addressing the imbalance of modality accessibility between training and inference.
- We innovatively define the virtual vision prediction as a multi-class classification task on a learnable codebook space, rather than traditional graph reconstruction or feature regression, which effectively alleviates the mean collapse issue often encountered in continuous output spaces and ensures that the generated virtual visual features are inherently discrete, thereby aligning naturally with the symbolic structure of expressions.
- We propose a pruning-based visualization technique that decomposes complex multivariate expressions into independent univariate sub-expressions. This allows each variable’s symbolic logic to be visualized as an independent 2D curve, thus facilitating the broader application of ViSymRe to multivariate SR problems.

In Section 2, the motivation underlying our work is outlined. In Section 3, we review the related work. Section 4 presents the proposed ViSymRe framework in detail, including its core components and implementation. Section 5 reports comparative evaluations against state-of-the-art baselines. Finally, Section 6 discusses the limitations of ViSymRe and outlines potential directions for future research.

## 2. Motivation

In recent years, pretrained SR models have drawn growing interest because they amortize inference. Once trained, a single forward pass can map a dataset to an expression, sidestepping the combinatorial search that makes traditional SR slow. Yet, despite borrowing architectures and training recipes from LLMs, these models have not reached similar convergence or robustness. A central reason is the modality gap. Datasets are unordered, noisy, and scale-dependent, while expressions are discrete, structured, and semantically sensitive. This mismatch makes model convergence difficult, leading to fragile generalization.

Our solution introduces the vision extracted by the expression graph as a bridging modality. Unlike the datasets, which are abstract and disordered, expression graphs exhibit explicit structural features. Each geometric primitive—such as straight line, parabola, S-curve, exponential curve, logarithmic curve, V-curve, bell-shaped curve, and waveform curve—corresponds to a specific symbol or symbol combination. By establishing correspondences from geometric primitives to symbols, the modality gap between datasets and expressions can be significantly bridged, thereby accelerating model convergence.

Furthermore, compared to the multimodal models in other fields, the multimodal SR model exhibits significant advantages in terms of lightweight and cost, for the following reasons:

- Expression graphs have geometric regularity and structural sparseness, allowing them to be represented at low resolution, and most of the pixels are 0, enabling feature extraction through a lightweight module.
- Both expressions and expression graphs can be automatically generated by computer programs, which eliminates the need for costly manual annotations, enabling unlimited and low-cost availability of training data.

## 3. Related work

**GP-based SR models** Traditional SR models are based on GP, which evolve expressions through simulating natural selection mechanisms [8]. While widely used, GP-based models are often inefficient, highly random, and sensitive to parameters. In recent years, several improved GP strategies have been developed, focusing on optimizing search efficiency and incorporating DL techniques [1, 9, 24, 10, 25, 12, 26]. Despite effectiveness, GP-based models are essentially search algorithms in a vast expression space, making it challenging to balance search quality and efficiency.

**DL-based SR models** Deep neural networks, with their powerful data fitting capabilities, have become widely used tools in the field of SR. Equation Learner (EQL) is an improved architecture based on fully connected neural networks, where the activation functions are replaced by operators [27]. While EQL inherits the data fitting capabilities of neural networks, special activation functions lead to training difficulties: division operation causes gradient explosion, periodic functions induce oscillation, and logarithmic and square root functions have non-differentiable regions. Deep Symbolic Regression (DSR) employs a recurrent neural network framework to predict the expression skeletons [14] (such as  $c + x^2$ , where  $c$  is a constant placeholder) in an autoregressive manner. By restricting physically meaningless couplings of symbols, DSR generates expressions with significantly lower complexity compared to GP-based and other DL-based models. However, this comes at the cost of reduced data fitting performance. PARFAM [16] represents expression as a coupled rational neural network, where the activation functions correspond to unary operations. PARFAM demonstrates strong performance in recovering polynomials but is insensitive to functions, resulting in some simple functions being replaced by more complex polynomial forms.

**Pretrained SR models** In response to the efficiency challenges widely present in SR, recent studies have drawn inspiration from the success of LLMs and introduced similar pretrained frameworks. Biggio et al. and Valipour et al. introduce the NeSymReS and SymbolicGPT, respectively, which prelearned the mapping from datasets to expression skeletons [17, 18], enabling fast skeleton inference. The remaining time cost is largely confined to using BFGS (Broyden-Fletcher-Goldfarb-Shanno) to regress the skeleton coefficients. To further improve efficiency, Kamienny et al. propose an end-to-end (E2E) framework that encodes constants as tokens, thereby achieving simultaneous prediction of expression skeletons and their constants [19]. Another method, SymFormer [20], achieves the same end-to-end capability by integrating a constant regression head at the end of the decoder.

Overall, pretrained SR models outperform GP-based and DL-based models in terms of efficiency. In addition, the expression search space of them can be further reduced by carefully designing the distribution of training expressions. However, they face similar generalization issues as in other fields, which is exacerbated by the insufficient convergence due to the modality gap between the datasets and expressions. Recently, several rectification strategies have been proposed, such as uDSR [28], TPSR [29], SNR [30], DGSR [31], SR-GPT [32]. These rectification strategies provide feedback on data fitting losses and complexity, allowing dynamic adjustments to the expression generation strategy. However, this comes at the cost of increased computational load and may cause the generated expressions to deviate from the desired distribution.

**Multimodal models** For a long time, machine learning has been used as a modeling tool for single modal, such as vision, text, and audio. The rise of deep learning has enabled multimodal learning. Early multimodal models typically mapped different modalities into a unified feature space through simple concatenation, element-wise operations, or feedforward networks [33, 34, 35]. The introduction of contrastive learning enables the effective alignment of different modalities before fusion, thereby significantly improving the performance of multimodal models [36, 37, 38]. ViLBERT [39] and LXMERT [40] introduce cross-attention fusion mechanisms that enable more effective interaction between vision and language, substantially improving joint representation learning. Generative models like DALL·E [41] demonstrates the capacity of large-scale multimodal transformer architectures to generate semantically coherent images. Imagen [42] further achieves state-of-the-art fine-grained semantic control by employing diffusion models with large-scale text-image pretraining. Recently, multimodal technology has also been introduced into SR. MMSR [21] considers the fusion representation of the dataset and symbol while employing the contrastive learning during the training process, achieving good data fitting results. However, the potential contribution of the visual modality in the field of SR has not yet been considered.

## 4. Method

ViSymRe comprises four main neural network modules for multimodal SR. The virtual visual encoder predicts virtual visual features from datasets, compensating for the absence of the visual modality during inference. The real visual encoder extracts and quantizes visual features from expression graphs while providing supervision for the virtual visual encoder. The dataset encoder focuses on extracting dataset features, and the multimodal SR module fuses visual and dataset features to predict the expression skeleton. Notably, during training, ViSymRe includes two multimodal SR modules with identical architecture and shared weights to ensure that real and virtual visual features jointly participate in skeleton prediction, which explicitly transfers the real visual prior to the virtual visual pipeline through parameter sharing, mitigating performance degradation caused by training-inference domain shift.

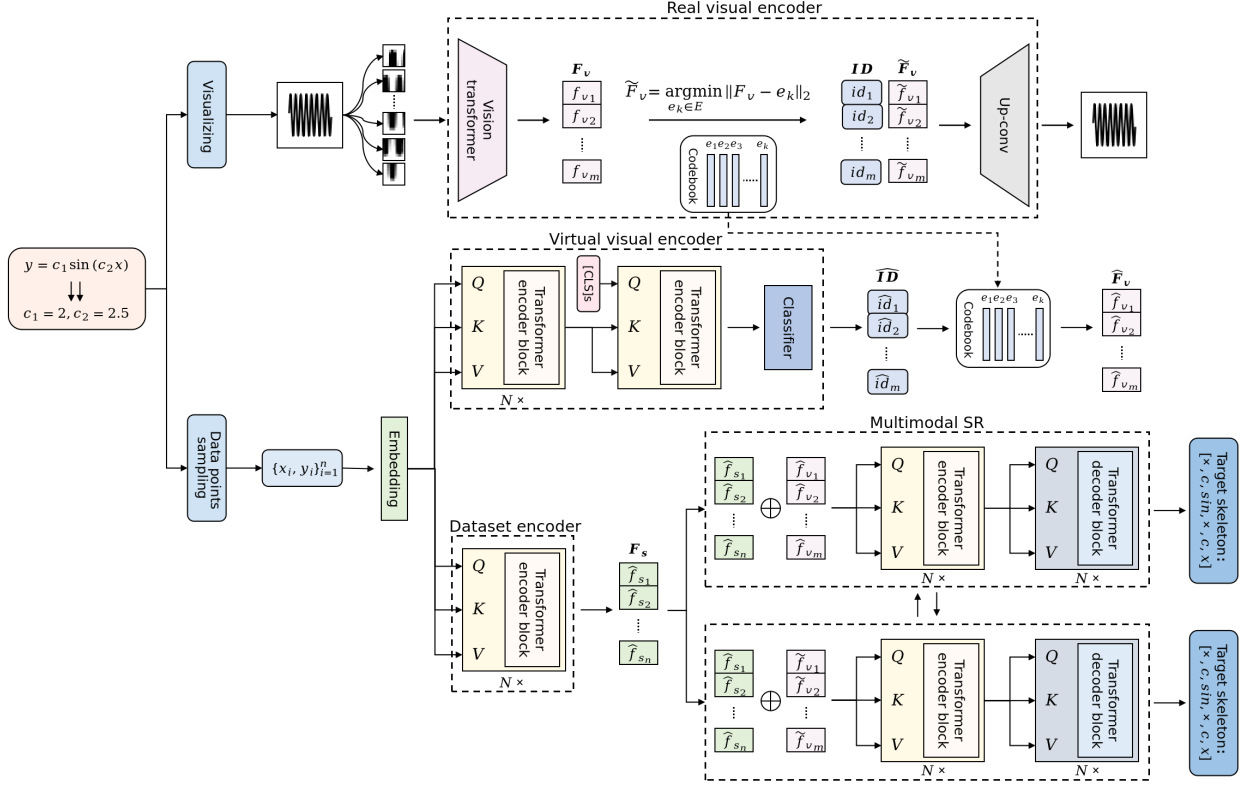


Figure 2: Overview of the ViSymRe framework. During training, all resources are available. ViSymRe fuses multi-source features to build a robust multimodal model. During inference, the expression graphs and real visual encoder are disabled. Visual features are entirely replaced by the predictions of the virtual visual encoder, thereby enabling graph-free multimodal SR.

As illustrated in Fig.2, ViSymRe supports both fully multimodal training and graph-free inference. In the following sections, we detail all modules, covering their functions, design principles, and key parameters.

#### 4.1. Expression pruning for visualization

For SR, there is no reference for defining vision. The core obstacles include unclear visualization targets (datasets or expressions) and imperfect visualization methods for high-dimensional problems. Some spatial transformation techniques, such as PCA, t-SNE, and UMAP, achieve discrete visualization by mapping high-dimensional datasets into lower-dimensional spaces. However, these techniques also have limitations. First, there is no unified method applicable to all problems. Selecting appropriate methods for different problems requires considering implementation costs and new evaluation metrics. Second, after dimensionality reduction, all variables are blended into the same space, obscuring the individual contributions of each variable, which makes it impossible to reveal symbolic relationships within the expression, contradicting our intention of using vision to bridge the modality gap. Moreover, we note that some methods inspired by the Kolmogorov–Arnold representation theorem can decouple high-dimensional datasets into a sum of univariate expressions, making them amenable to visualization [43]. However, these methods typically require additional spline/basis coefficient optimization and post-processing, which increases training and inference costs. Importantly, the resulting curves may not strictly reflect the symbolic logic of the original expressions..

Therefore, we redefine the visualization target to focus directly on the symbolic logic of expressions. One feasible approach is to fix the value of some variables at a constant (usually 1) while varying one variable at a time, thereby obtaining the curve that shows how this variable influences the target. However, this method is not without its flaws. For example, a special three-variable expression  $f(x_1, x_2, x_3) = x_1(x_2 - x_3)$ .  $f(x_1, 1, 1)$  remains zero regardless of  $x_1$ , which hinders the generalization of the method.

For visual SR, an ideal visualization system should satisfy the following three properties:

1. Ensure a one-to-one mapping between expression skeletons and graphs
2. Maintain the correspondences between geometric primitives and symbols, as discussed in Section 2.
3. Multivariable expression graphs should be decoupled into independent parts, each of which illustrates the impact of one variable on the target.
4. The graphs should not be affected by constants in expressions to avoid introducing continuity.

It is clear that existing 2D visualizations already satisfy properties 1 and 2. To achieve graph decoupling and discretization, we design a pruning algorithm (Algorithm 1), which prunes multivariable expressions into multiple univariate forms while preserving all symbolic operations related to the specified variable and removing all constants. The detailed pruning process is as follows:

- Designate a variable as the specified variable.
- Recursively traverses each part of the expression. An element is pruned if it meets the following conditions:
  - It is a constant.
  - It is not the specified variable.
  - It is not the symbol related to the specified variable.

To ensure the integrity of the expressions, the pruned parts (elements) are replaced with neutral elements according to their parent nodes (0 for addition and subtraction, and 1 for multiplication and division).

---

**Algorithm 1** Dependency query algorithm

---

```

1: Input:  $g$  (node/subtree),  $spec\_var$  (specified variable)
2: Output: true or false
3: function DEPQUERY( $g$ ,  $spec\_var$ )
4:   if  $g \in Constant$  then
5:     return false
6:   else if  $g \in Variable$  then
7:     return ( $g = spec\_var$ )
8:   else if  $g$  is a sum ( $\sum_i$ ) or product ( $\prod_j$ ) then
9:     for all child  $h$  of  $g$  do
10:      if DEPQUERY( $h$ ,  $spec\_var$ ) then
11:        return true
12:      end if
13:    end for
14:    return false
15:   else if  $g$  is an exponentiation  $g = base^{exp}$  then
16:     return DEPQUERY(base,  $spec\_var$ )
17:   else if  $g$  is a unary operator  $g = Una\_op(h)$  then
18:     return DEPQUERY( $h$ ,  $spec\_var$ )
19:   else
20:     return false
21:   end if
22: end function

```

---

For an expression containing  $d$  variables, we iteratively apply Algorithm 2  $d$  times,  $x_i, i = 1, 2, \dots, d$  as the specified variable in the  $i$ -th iteration, with the pruned expression denoted as  $f_i$ . We visualize  $(x_i, f_i(x_i))$  in 2D space so that the graph satisfies properties 1, 2, and 4. Then, use grayscale technology to convert the graph to a single channel, and apply binarization (0 or 1) to make the curves clearer. Finally, all graphs about  $d$  variables are stacked along the channel dimension to obtain a composite graph that satisfies property 3.

---

**Algorithm 2** Pruning algorithm

---

```
1: Input:  $f$  (expression with  $d$  variables);  $spec\_var$  (specified variable)
2: Output:  $\hat{f}$  (expression pruned to depend only on  $spec\_var$ )
3: function PRUNE( $f, spec\_var$ )
4:   if  $f$  is a sum  $f = \sum_{i=1}^n a_i$  then // Recursively handle +/- using identity 0
5:      $\mathcal{A} \leftarrow []$ 
6:     for all  $a_i$  in  $f$  do
7:       if DEPQUERY( $a_i, spec\_var$ ) then
8:          $\mathcal{A}.append(PRUNE(a_i, spec\_var))$  // Call (Algorithm. 1)
9:       else
10:         $\mathcal{A}.append(0)$ 
11:      end if
12:    end for
13:    return  $\sum_{k=1}^{|\mathcal{A}|} \mathcal{A}[k]$ 
14:  else if  $f$  is a product  $f = \prod_{j=1}^m m_j$  then // Recursively handle  $\times/\div$  using identity 1
15:     $\mathcal{M} \leftarrow []$ 
16:    for all  $m_j$  in  $f$  do
17:      if DEPQUERY( $m_j, spec\_var$ ) then
18:         $\mathcal{M}.append(PRUNE(m_j, spec\_var))$ 
19:      else
20:         $\mathcal{M}.append(1)$ 
21:      end if
22:    end for
23:    return  $\prod_{k=1}^{|\mathcal{M}|} \mathcal{M}[k]$ 
24:  else if  $f$  is an exponentiation  $f = b^e$  then //  $e$  is constant and always kept
25:     $b' \leftarrow PRUNE(b, spec\_var)$  if DEPQUERY( $b, spec\_var$ ) else 1
26:    return  $(b')^e$ 
27:  else if  $f$  is a unary operator  $f = \text{Una\_op}(g)$  then
28:    return  $\text{Una\_op}(PRUNE(g, spec\_var))$  // Preserve the unary operator and prune its operand.
29:  else
30:    return  $f$  // Leaf node: variable or constant
31:  end if
32: end function
```

---

## 4.2. Real visual encoder

Currently, mainstream multimodal models regard the visual encoder as a purely feedforward component that is jointly optimized with other modules via a shared training objective. However, for ViSymRe, the real visual encoder not only directly contributes to the visual feature extraction but also provides supervision for the virtual visual encoder during training. To support this dual role, we define it as an autoencoding module, allowing it to be optimized independently.

Specifically, we first perform forward visual encoding using a Vision Transformer (ViT) without the classification head, which divides the expression graph into  $m$  patches and generates  $m$  visual features through self-attention. Then, the visual features are quantized in a learnable codebook space, aiming to discretize the continuous feature space. This process is formulated as:

$$\widetilde{f}_{v_i} := \arg \min_{e_k \in E} \|f_{v_i} - e_k\|_2, \quad \text{for } i = 1, \dots, m, \quad (1)$$

where the  $F_v = [f_{v_1}, f_{v_2}, \dots, f_{v_m}]$  and  $\widetilde{F}_v = [\widetilde{f}_{v_1}, \widetilde{f}_{v_2}, \dots, \widetilde{f}_{v_m}]$  represent original and quantized visual features respectively,  $E = \{e_1, e_2, \dots, e_k\}$  is the codebook space containing  $K$  learnable vectors, and  $\|*\|_2$  is the Euclidean distance. The quantization loss is described as:

$$\mathcal{L}_{Quan} = \beta \|F_v - sg[\widetilde{F}_v]\|_2^2 + \|sg[F_v] - \widetilde{F}_v\|_2^2, \quad (2)$$

where the first term is commitment loss and the second term is codebook loss, which are used to update the real visual encoder and codebook, respectively, to encourage the visual features to be as close as possible to their corresponding codebook vectors. The  $\beta$  is a hyperparameter that controls the weight of commitment loss in the total loss. We set  $\beta = 0.1$ . Since quantization is non-differentiable, a straight-through estimator with the stop-gradient operator  $sg[*]$  is used to enable backpropagation.

In addition, a complete autoencoding process also includes an upsampling decoder and an additional reconstruction loss. Since the pixel values of the expression graphs are either 0 or 1, we use binary cross-entropy (BCE) to define the reconstruction loss, as described below:

$$\mathcal{L}_{Recon} = - \sum_i [G_i \log(\hat{G}_i) + (1 - G_i) \log(1 - \hat{G}_i)], \quad (3)$$

where the  $G$  represents the expression graphs, and the  $\hat{G} = Decoder(\widetilde{F}_v)$  represents the reconstructed ones.

### 4.2.1. Dataset encoder

In the field of SR, the input dataset is denoted as a set of data points  $D = \{X_i, y_i\}_{i=1}^n \in R^{n \times (d+1)}$ , where  $d$  and 1 represent the number of variables and target respectively, and  $n$  indicates the number of data points. Since the data points may take extremely large or small values, leading to numerical instability, normalization is necessary. However, commonly used methods, such as Min-Max and Z-score, destroy the internal structure of the dataset, thereby hindering the SR model’s ability to capture the relationships between variables and targets accurately. To address this problem, E2E [19] applies a post-hoc remapping strategy that reprojects the variables in the generated expressions back to the original scale, but at the cost of increased expression complexity. Inspired by NeSymReS[17], we adopt an IEEE-754-based normalization, which encodes each floating point number as a multi-bit binary representation composed of one sign bit, eight exponent bits, and eight mantissa bits (see Appendix C for details). After normalization, the shape of the dataset is changed to  $R^{n \times ((d+1) \times 17)}$ .

We employ a Transformer module with a Pre-Layer Normalization (Pre-LN) architecture to serve as the dataset encoder, which facilitates stable gradient flow and convergence during training. In addition, we refer to the following attention regularization mechanism [44] to avoid the numerical instability problem that may occur during FP16-precision training.

**Attention regularization:** The standard scaled dot-product attention score is computed as follows:

$$\text{Attn}(Q, K, V) = \text{softmax}\left(\frac{QK^T}{\sqrt{d}}\right)V, \quad (4)$$

where  $Q$ ,  $K$ , and  $V$  represent the query, key, and value matrices, respectively, and  $d$  is the dimension of the key vectors. However, under low-precision training, the inner product  $QK^T$  may produce abnormally large values, leading to numerical overflow or instability during the softmax computation. To mitigate this issue, we adopt a stabilized computation strategy: instead of directly computing  $QK^T / \sqrt{d}$ , we first scale the key matrix, i.e., compute  $Q(K^T / \sqrt{d})$ , which reduces the likelihood of early numerical explosion without altering the result. Moreover, leveraging the equation:  $\text{softmax}(Q(K^T / \sqrt{d})) = \text{softmax}(Q(K^T / \sqrt{d}) - \text{constant})$ , we further subtract the row-wise maximum from the attention logits, resulting in the following numerically stabilized form:

$$\text{Attn}(Q, K, V) = \text{softmax}\left(\left(Q\left(\frac{K^T}{\alpha\sqrt{d}}\right) - \max\left(Q\left(\frac{K^T}{\alpha\sqrt{d}}\right)\right)\right)\alpha\right), \quad (5)$$

where  $\alpha$  is a settable rescaling constant (e.g.,  $\alpha = 10^3$ ), introduced to maintain numerical precision while preventing gradient underflow or overflow. Note that the output distribution of  $\text{softmax}(\cdot)$  is not affected by  $\alpha$  due to its invariance to multiplicative constants. Thus, the value of  $\alpha$  is not sensitive and can be safely fixed during training. Overall, this regularization method is simple yet effective in ensuring stable attention computations under low-precision settings, and it can be easily integrated into standard attention implementations with minimal overhead.

#### 4.2.2. Virtual visual encoder

Traditional vision multimodal models typically require graph availability throughout both training and inference to access real-time visual modalities. However, in the field of SR, expression graphs are unavailable during inference, which limits the model to rely solely on the dataset. Our research hypothesizes that the multimodal capabilities of the model learned from expression graphs available during training can be effectively generalized to scenarios where graphs are unavailable during inference.

We design an end-to-end module, termed the virtual visual encoder, which is trained to predict the indices in the codebook space of the quantized visual features output by the real visual encoder, conditioned on the dataset. It first extracts high-level dataset representations through multi-layer Transformer block, and then performs cross-attention with a set of  $m$  learnable query vectors, where  $m$  corresponds to the number of patches in the expression graph. This operation yields  $m$  parallel classification heads, each mapped to a codebook index via a shared nonlinear classifier. The resulting indices are used to retrieve codebook vectors from the codebook, referred to as virtual visual features, which are subsequently integrated into the multimodal fusion process.

The advantage of our approach lies in transforming the regression problem, which is optimized in a continuous space, into a multi-class classification problem in a discrete space, thereby enabling the virtual visual encoding loss to be defined using the more stable cross-entropy objective:

$$\mathcal{L}_{VVE} = -\frac{1}{m} \sum_{p=1}^m \log \frac{\exp(\pi_{p, \text{id}_p})}{\sum_{k=1}^K \exp(\pi_{p,k})}, \quad (6)$$

where  $\pi_{p,k}$  denotes the logit of the  $p$ -th classification head for the  $k$ -th codebook vector,  $\text{id}_p \in \{1, \dots, K\}$  is the ground-truth codebook index obtained from the real visual encoder, and  $K$  is the codebook size. This effectively alleviates graph blurring and feature degradation issues commonly observed in MSE-based regression [22]. Moreover, another advantage of our approach is that it performs the inference process from graph to expression into a discrete-to-discrete mapping, analogous to language-to-language translation, thereby facilitating input-output alignment.

### 4.3. Multimodal SR module

#### 4.3.1. Multimodal fusion and alignment

ViSymRe adopts a simple yet effective modality fusion strategy: the  $m$  visual features and  $n$  dataset features are directly concatenated into a unified sequence with length  $m + n$ , which is then processed by multi-layer Transformer block for joint representation learning.

Moreover, considering the inherent differences between visual and dataset features, direct fusion without alignment may lead to confusion, thus degrading the multimodal performance. To address this issue, we introduce contrastive learning [37], which imposes constraints on multi-source features to enforce alignment through the following loss function:

$$\begin{aligned} \mathcal{L}_{CL} = & -\frac{1}{N} \sum_{i=1}^N \log \left( \frac{\exp(s_i^T v_i / \tau)}{\sum_{j=1}^N \exp(s_i^T v_j / \tau)} \right) \\ & -\frac{1}{N} \sum_{i=1}^N \log \left( \frac{\exp(v_i^T s_i / \tau)}{\sum_{j=1}^N \exp(v_i^T s_j / \tau)} \right). \end{aligned} \quad (7)$$

Here,  $s_i$  and  $v_j$  denote the dataset and visual features, respectively, projected and normalized into the same embedding space. if  $i = j$ , it is called a positive sample pair, and if  $i \neq j$ , it is called a negative sample pair.  $\tau$  is a temperature parameter controlling the concentration level of the similarity distribution. By simultaneously maximizing the similarity of positive pairs and minimizing the similarity of negative pairs, multimodal alignment is achieved before fusion.

#### 4.3.2. Decoder

Expression decoding is performed autoregressively using a Transformer decoder, following the pre-order traversal of the expression tree to ensure that the generated expressions are both logically coherent and mathematically valid. Furthermore, we recognize that the structural reasonableness of the expressions is critical for subsequent mechanism analysis. Not all expressions are physically meaningful or valid. For instance, simple structures like  $\cos(\sin(x))$  or more complex structures like  $\exp^{\exp(\cos(x))}$  often don't correspond to any physical law [14]. However, due to their strong fitting capability to datasets, such expression structures are prone to being generated by SR models. To address this issue, we develop a constraint strategy that functions by actively monitoring the ancestor nodes of the current position during the decoding process to adjust the probability of outputting certain symbols (see Algorithm 3). The presence of risky operators (such as exponential and trigonometric functions) at the ancestor nodes is a key indicator that irrational nesting might occur in subsequent steps. As a constraint, if any suspicious ancestor nodes are detected during decoding, the probability of outputting symbols that might lead to unreasonable nesting will be set to 0.

#### 4.4. Optimization

ViSymRe is optimized by two principal losses: the real visual encoding loss  $\mathcal{L}_{RVE}$  and the multimodal SR loss  $\mathcal{L}_{MMSR}$ .

The  $\mathcal{L}_{RVE}$  is formulated as the sum of the quantization loss  $\mathcal{L}_{Quan}$  (refer to Eq. 2) and the reconstruction loss  $\mathcal{L}_{Recon}$  (refer to Eq. 3):

$$\mathcal{L}_{RVE} = \mathcal{L}_{Quan} + \mathcal{L}_{Recon}. \quad (8)$$

The  $\mathcal{L}_{MMSR}$  is defined as:

$$\mathcal{L}_{MMSR} = \mathcal{L}_{RSP} + \mathcal{L}_{VSP} + \mathcal{L}_{VVE} + \lambda_{CL} \mathcal{L}_{CL} + \lambda_{Cons} \mathcal{L}_{Cons}, \quad (9)$$

where  $\mathcal{L}_{CL}$  (refer to Eq. 7) is the contrastive learning loss.  $\mathcal{L}_{RSP}$  and  $\mathcal{L}_{VSP}$  are the expression skeleton prediction loss of real and virtual visual pipeline, respectively, and  $\mathcal{L}_{VVE}$  (refer to Eq. 6) is the virtual visual encoding loss. In addition, to promote the consistency of the skeleton distribution predicted by the real and virtual visual pipelines, we define the consistency loss ( $\mathcal{L}_{Cons}$ ) through the following KL divergence:

$$\mathcal{L}_{Cons} = \mathbb{E}_i \left[ \text{KL}(\mathbf{p}_i^{(r)} \parallel \mathbf{p}_i^{(v)}) \right], \quad (10)$$

where  $\mathbf{p}_i^{(r)}$  and  $\mathbf{p}_i^{(v)}$  denote the symbol probability distributions at position  $i$  output by the real and virtual visual pipeline, respectively.  $\lambda_{CL} = \lambda_{Cons} = 0.1$  are scalar balancing coefficients for  $\mathcal{L}_{CL}$  and  $\mathcal{L}_{Cons}$ , respectively.

Furthermore, a major challenge in jointly optimizing the virtual visual encoder with other modules is that the arg max operation, used to index the codebook vector from the codebook space, is non-differentiable and thus blocks gradient flow. Therefore, we adopt the Gumbel-Softmax relaxation [45], which provides a differentiable approximation to discrete sampling:

$$\hat{\mathbf{d}}_i = \sum_{k=1}^K \frac{\exp((\pi_{i,k} + g_k)/\tau)}{\sum_{l=1}^K \exp((\pi_{i,l} + g_l)/\tau)} o_k, \quad (11)$$

---

**Algorithm 3** Ancestor nodes search algorithm

---

```
1: Input:  $\mathcal{T}$ : prefix token sequence of the current expression tree
2: Output:  $\mathcal{N}$ : stack of ancestor nodes
3: function SEARCHANCESTORNODES( $\mathcal{T}$ )
4:    $\mathcal{N} \leftarrow []$  // Ancestor stack
5:   child  $\leftarrow []$  // Remaining children for each ancestor
6:   for token  $t$  in  $\mathcal{T}$  do
7:     if  $t \in [\sin, \cos, \tan, \arcsin, \exp, \log, \sqrt{\phantom{x}}, \text{pow}]$  then
8:        $\mathcal{N}.\text{append}(t)$ 
9:       child.append(1)
10:    else if  $t \in [+ , - , * , /]$  then
11:       $\mathcal{N}.\text{append}(t)$ 
12:      child.append(2)
13:    else if  $t \in \{\text{Variable}, \text{Constant}\}$  then
14:      if child  $\neq \emptyset$  then
15:        child[-1]  $\leftarrow$  child[-1] - 1 // Consume one child of the current ancestor
16:      end if
17:    end if
18:    while child  $\neq \emptyset$  and child[-1] = 0 do
19:       $\mathcal{N}.\text{pop}()$  // Close the finished subtree
20:      child.pop()
21:      if child  $\neq \emptyset$  then
22:        child[-1]  $\leftarrow$  child[-1] - 1
23:      end if
24:    end while
25:  end for
26:  return  $\mathcal{N}$  // Ancestor nodes at the current decoding position
27: end function
```

---

where  $\pi_{i,k}$  is the logit output of the  $i$ -th classification head for the  $k$ -th codebook vector,  $o_k$  is the  $k$ -th one-hot basis vector, and  $\tau$  is the temperature parameter controlling the smoothness of the distribution. During training,  $\tau$  is gradually annealed from 1 to 0 to enable a smooth transition from soft to hard assignments. The Gumbel noise  $g_k$  is sampled from Gumbel(0, 1) via  $g_k = -\log(-\log u_k)$ , where  $u_k \sim \text{Uniform}(0, 1)$ .

## 5. Experimental results

In this section, we compare ViSymRe with state-of-the-art SR baselines on multiple benchmarks to evaluate its effectiveness and robustness, with the details presented in the following subsections.

### 5.1. Dataset

**Training set:** The expression skeletons required for training ViSymRe are pre-generated, totaling 10 million. To improve ViSymRe’s generalization ability, we introduce variability by randomly sampling constants and data points for each skeleton, ensuring coverage of a wide range of numerical scales. For details on the expression skeleton generation process and the sampling strategies for constants and data points, please refer to Appendix A.

**Testing benchmarks:** To comprehensively evaluate the performance of ViSymRe in various SR scenarios, we conducted experiments on the following widely used benchmarks:

- **Low-dimensional benchmarks:** The low-dimensional benchmarks include "Nguyen" [46], "Keijzer"[47], "Korns" [48], "Constant", "Livermore" [14], "Jin" [49] and "Neat". These benchmarks contain SR problems with up to three variables.

- **SRBench [50]:** The SRbench contain 133 ground-truth problems from the following two databases:
  - **Feynman database [12]:** The Feynman database comes from first principles models of physical systems, consisting of 119 real-world expressions from the Feynman Lectures on Physics [51], paired with sampled datasets for each expression.
  - **ODE-Strogatz database [52]:** The ODE-Strogatz database includes a variety of nonlinear dynamical systems, some of which exhibit chaotic behavior. It comprises 14 problems, each modeling the time evolution of a two-dimensional system governed by coupled first-order ordinary differential equations.
- **SRSF-Feynman benchmark [53]:** SRSF-Feynman is an improved version of the Feynman database that redefines the sampling ranges of coefficients and variables in expressions to reflect typical experimental settings and physical scales more accurately.
- **Randomly generated skeletons:** We randomly generated several synthetic datasets, each comprising 200 symbolic skeletons. To support the ablation analysis of the model, we preset the skeleton complexity (the number of variables, unary operators, and constants) and the number of sampled test points.

### 5.2. Training details

We divide the training of ViSymRe into two stages. First, the real visual encoder is trained for five epochs according to Eq. 8. After it converges, its parameters are frozen to stabilize the codebook. Then, the remaining modules, including the virtual visual encoder, dataset encoder, and multimodal SR, are trained according to Eq. 9 until convergence on the validation set.

The device used to train ViSymRe is an Intel(R) Core(TM) i5-13600K CPU @ 3.50 GHz with 32 GB RAM, equipped with an NVIDIA RTX 5070 Ti GPU (16 GB). One epoch takes approximately 5 hours.

### 5.3. Testing details

Since the number of data points included in the input dataset is limited during training, the performance of ViSymRe may descend when the number of test points significantly exceeds this threshold. We select  $B$  bags, each of which is a random subset of the test points. For each bag, we apply beam search to generate  $C$  candidate expression skeletons. Then, the BFGS algorithm is employed to optimize the constants within them. Additionally, we simplify the candidate expressions by removing terms with extremely small coefficients, as these may represent potential noise. Finally, the candidate expression with the highest fitting degree is determined as the final result.

### 5.4. Baselines

We compare ViSymRe with the following baselines, including four recently proposed dataset-only pretrained models and several representative GP-based and DL-based models.

- **NeSymReS [17]:** A pretrained Transformer-based autoregressive architecture that represents a classic paradigm of pretrained SR models. It treats operators (i.e., ' $exp$ ', ' $sin$ ',  $\dots$ ), constants, and variables as tokens and generates expressions following the preorder traversal of a binary tree.
- **E2E [19]:** A pretrained model with end-to-end capability, supporting constant encoding and high-dimensional problems.
- **SymFormer [20]:** Another implementation mode of end-to-end SR that uses a regression head to predict constants instead of the encoding and decoding process.
- **TPSR [29]:** An improved version of E2E, incorporating Monte Carlo Tree Search (MCTS) as a rectification strategy to enhance the generalization ability.
- **PySR [26]:** The PySR represents a new trend in GP-based SR models. It employs a multi-objective, highly parallel evolutionary algorithm and integrates a noise filter, aiming to achieve robust, efficient, and interpretable SR.

- **SRBench Baselines [50]:** The 7 best-performing open-source SR models reported in SRBench ( including AFP\_PE [9], AIFeynman [12], AFP [9], ITEA [54], DSR [14], EPLEX [10] and Gplearn), which represent the mainstream performance in the field of SR.

To ensure reproducibility, all parameters used by the pretrained and SRBench baselines are set to the default values provided by the authors. For PySR, we refer to the settings of [53].

### 5.5. Metrics

In our experiments, there are four metrics to evaluate the models’ performance:

- **$R^2$  score:**  $R^2$  score measures how well the predicted expression fits the dataset. Its formula is described as:

$$R^2 = 1 - \frac{\sum_{i=1}^n (y_i - \hat{y}_i)^2}{\sum_{i=1}^n (y_i - \bar{y})^2}, \quad (12)$$

If  $R^2 \geq 0.999$ , the predicted expression is considered to fit the dataset accurately.

- **Complexity:** Complexity is the number of symbols in expressions. If an expression fits the dataset accurately and is simple, it is considered to be a good expression.
- **Symbolic solution rate:** Symbolic solution aims to identify the predicted expression that differs from the ground-truth one by a constant or scalar. It is first introduced by [50], and defined as follow:

**Definition 1.** A predicted expression  $\hat{f}$  is considered as a symbolic solution to a problem with the ground-truth expression  $f + \epsilon$ , if  $\hat{f}$  does not simplify to a constant, and at least one of the following conditions holds:

- $f = \hat{f} + \alpha$ , where  $\alpha$  is constant;
- $f = \hat{f}/\beta$ , where  $\beta$  is constant and  $\beta \neq 0$ .

Compared to the  $R^2$  score, which focuses on numerical accuracy, the symbolic solution provides a deeper assessment of a model’s ability to capture the actual expression structure.

The symbolic solution rate represents the proportion of symbolic solutions identified by SR model.

- **Normalized edit distance (NED):** The edit distance computes the minimum number of insertions, deletions, and substitutions required to transform one expression tree to another [53]. To account for varying expression complexity, it is normalized as:

$$\bar{d}(f, \hat{f}) = \min\left(1, \frac{d(\mathcal{T}(f), \mathcal{T}(\hat{f}))}{|\mathcal{T}(f)|}\right), \quad (13)$$

where the  $|\mathcal{T}(f)|$  denotes the number of nodes in the ground-truth expression tree. NED offers a continuous, coefficient-insensitive measure of expression structural similarity, making it more suitable for complex scenarios than symbolic solution.

### 5.6. Results on low-dimensional benchmarks

In SR, low-dimensional problems cover the majority of practical scenarios. Therefore, we comprehensively evaluate ViSymRe on low-dimensional benchmarks. The comparison are NeSymReS, E2E, SymFormer, TPSR and PySR. Each experiment is repeated 10 times and averaged to ensure statistical significance.

We first evaluated the models’  $R^2$  score and complexity, which are considered the basic metrics for measuring SR performance. The results are shown in Table 1. It can be observed that ViSymRe maintains optimal or suboptimal  $R^2$  score on all benchmarks, and the complexity achieved is significantly lower than that of others, reflecting its ability to balance data fitting with interpretability, an essential property for real-world scientific discovery. In comparison,

Table 1: The mean  $R^2$  score and complexity results on low-dimensional benchmarks.

Benchmarks	ViSymRe		PySR		NeSymReS		E2E		TPSR		SymFormer	
	Mean $R^2$	Compl.	Mean $R^2$	Compl.	Mean $R^2$	Compl.	Mean $R^2$	Compl.	Mean $R^2$	Compl.	Mean $R^2$	Compl.
Constant	<b>0.9999</b>	<b>9.29</b>	0.9996	21.56	0.9443	10.87	0.8205	22.37	0.9298	27.25	0.9090	12.79
Jin	<b>0.9999</b>	<b>12.77</b>	<b>0.9999</b>	19.72	0.9018	13.50	0.9613	27.83	<b>0.9999</b>	22.50	0.9408	21.27
Keijzer	<b>0.9999</b>	<b>9.35</b>	0.9990	18.92	0.8745	10.76	0.9954	20.73	0.9707	20.35	0.8411	20.46
Korns	<b>0.9999</b>	<b>10.85</b>	0.9993	19.71	0.8200	11.76	0.9201	22.38	0.9982	16.77	0.8355	14.52
Livermore	<b>0.9999</b>	<b>8.72</b>	<b>0.9999</b>	15.93	0.9238	9.48	0.8638	22.09	0.9517	23.72	0.9156	13.26
Neat	<b>0.9999</b>	<b>10.33</b>	0.9998	20.66	0.7638	11.91	0.9732	21.37	0.9986	21.83	0.8015	19.54
Nguyen	0.9989	<b>9.25</b>	<b>0.9999</b>	13.68	0.9678	10.19	0.9963	19.47	0.9998	21.08	0.9846	16.16
Nguyen'	<b>1.0000</b>	<b>7.16</b>	0.9999	15.66	0.9957	7.91	0.9996	14.91	0.9998	14.75	0.9985	19.50
Nguyen''	<b>0.9999</b>	<b>10.26</b>	<b>0.9999</b>	16.60	0.9990	10.53	<b>0.9999</b>	10.8	<b>0.9999</b>	12.73	0.9959	19.86

NeSymReS also generates relatively simple expressions, ranking second in complexity, but its  $R^2$  score drops substantially on several benchmarks, a weakness similarly observed in SymFormer. PySR and TPSR are competitive in  $R^2$  score, but their complexity is almost twice that of ViSymRe, which reduces the interpretability of expressions.

Beyond  $R^2$  score and complexity, a key goal of SR is to recover the underlying symbolic structure of the ground-truth expression. Fig. 3 reports the NED results for evaluating the model’s ability to recover real expression structure. As can be seen, ViSymRe obtains the lowest NED on all benchmarks, underscoring its ability to not only fit data well but also uncover expressions that closely match the true underlying structure. PySR, SymFormer, and NeSymReS form the second tier. Although they achieve NED comparable to ViSymRe on some benchmarks, a gap remains. For other models, the NED is generally higher than 0.5, indicating that they emphasize data fitting at the expense of structural accuracy, making them more akin to black-box learners.

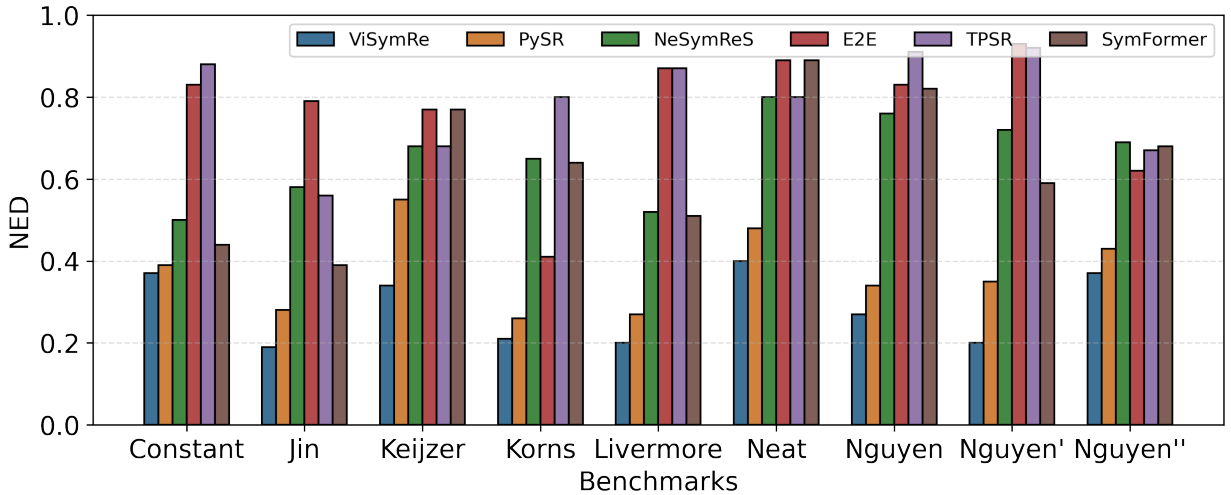


Figure 3: The NED results on low-dimensional benchmarks. ViSymRe achieves the lowest NED on all benchmarks, while other models show higher values, indicating their stronger tendency to prioritize data fitting over structural accuracy.

To evaluate the robustness of the models under different noise levels, we recorded the changes in each model’s

$R^2$  score and NED at three noise intensities (0, 0.01, and 0.1). For ease of visualization, the results are averaged over all nine low-dimensional benchmarks, as shown in Fig. 4. Overall, higher noise degrades all models, but ViSymRe consistently preserves both high  $R^2$  and low NED, with only smooth declines even at the noise level of 0.1. Although PySR and TPSR exhibit a high  $R^2$  score on clean data, they drop sharply once noise increases. NeSymReS, E2E, and SymFormer degrade even faster, retaining their  $R^2$  scores less than half of those on clean data at the noise level of 0.1. These results highlight the robustness of ViSymRe to noise, which is essential for practical applications of SR in real-world scientific discovery, where experimental data rarely achieve ideal noiseless conditions.

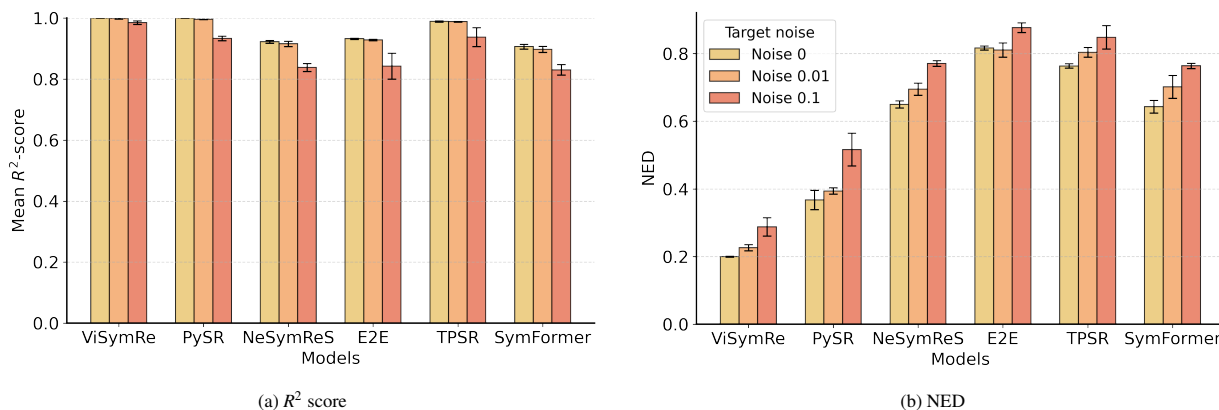


Figure 4: Robustness of models under varying noise levels. Results are averaged over nine low-dimensional benchmarks, showing the changes in  $R^2$  score and NED at three noise intensities (0, 0.01, and 0.1). We can see that ViSymRe consistently maintains higher  $R^2$  score and lower NED than the baselines as noise increases.

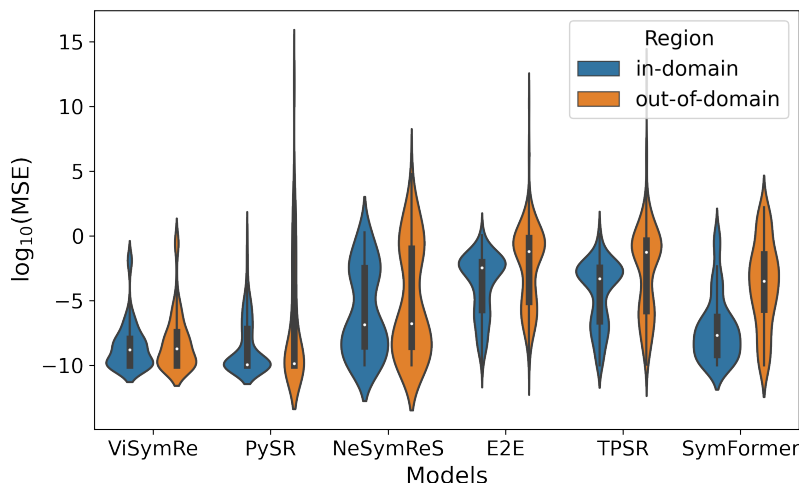


Figure 5: Error distributions of ViSymRe, PySR, and TPSR on in-domain and out-of-domain datasets. While all models fit the in-domain data well, only ViSymRe maintains a similar error distribution under dataset shift, indicating its superior extrapolation capability compared to the baselines.

Extrapolation capability is a critical aspect of SR, as it reflects a model’s ability to generalize beyond the observed datasets. We evaluate the extrapolation capabilities of ViSymRe and baselines on low-dimensional benchmarks. The datasets used for generating expressions are defined as in-domain datasets, based on which we expand the sampling range by a factor of two to create the out-of-domain datasets. For expressions generated by each model that achieved  $R^2 > 0.999$  on the in-domain dataset, we record the MSE of them on both in-domain and out-of-domain datasets, and show the distribution in Fig. 5. It can be seen that the MSE distributions of ViSymRe on in-domain and out-of-domain datasets are highly overlapping, with the center remaining roughly around  $10^{-10}$  and the spread being minimal,

demonstrating stable extrapolation capabilities. NeSymReS and SymFormer exhibit moderate extrapolation, with similar MSE distributions across in-domain and out-of-domain datasets. The MSE distributions of E2E, TPSR, and PySR exhibit clear shifts and substantial widening on the out-of-domain dataset compared to those on the in-domain dataset, with the centers moving up by several orders of magnitude. Among them, PySR has the most pronounced long tail and the least stable extrapolation. Overall, the results indicate that a high  $R^2$  score alone does not guarantee reliable extrapolation. Although some increase in MSE under distribution shift is inevitable, ViSymRe maintains higher consistency, demonstrating stronger extrapolation robustness, which further suggests that ViSymRe tends to capture the underlying expression structure rather than merely fitting the data.

The comprehensive radar chart (Fig. 6) illustrates the overall performance of each model across four key metrics:  $R^2$  score, NED, complexity, and test time. To ensure comparability, all results are normalized to a range of 0 to 1. As shown, ViSymRe maintains strong performance across all dimensions, indicating that it achieves a good balance in various SR capabilities. Other models tend to specialize in certain aspects but reveal clear weaknesses elsewhere. For instance, PySR and TPSR achieve relatively high  $R^2$  scores but suffer from higher complexity and longer inference times. NeSymReS generates simpler expressions but sacrifices robustness in the  $R^2$  score. E2E is efficient in terms of test time, but less competitive in terms of NED and complexity. These results highlight that while individual baselines may excel in isolated metrics, ViSymRe provides a more comprehensive solution by maintaining equilibrium across multiple metrics, making it better suited for real-world SR tasks.

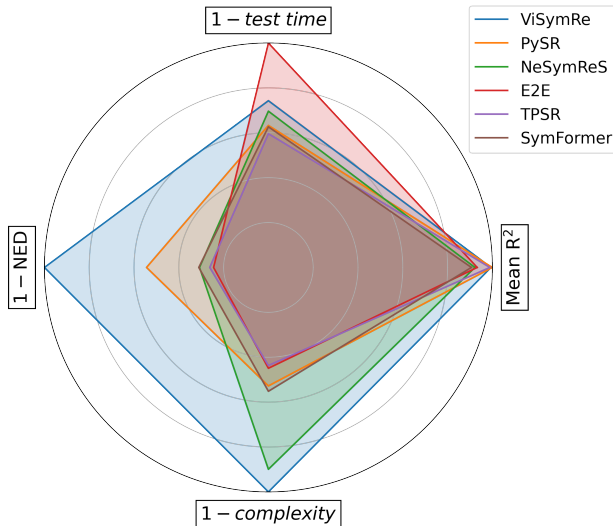


Figure 6: Radar chart of overall model performance across  $R^2$  score, NED, complexity, and test time (all normalized to [0,1]). ViSymRe achieves a well-balanced performance across all dimensions, in contrast to baselines that display competitiveness in certain aspects yet suffer from notable shortcomings in others.

### 5.7. Results on SRBench

In this section, we evaluate ViSymRe on SRBench [50], including 119 Feynman problems [12] and 14 ODE-Strogatz problems [52]. Each dataset is split into 75% training data and 25% test data. To ensure fairness and consistency in evaluation, we use the metrics reported in SRBench, including accuracy solution rate (i.e., the proportion of predicted expressions achieving an  $R^2$  score > 0.999), symbolic solution rate, and complexity. The SRBench baselines and PySR are used for comparison.

Fig. 7a presents the models' evaluation results on 119 Feynman problems. As shown, ViSymRe achieves the highest accuracy and symbolic solution rates across all noise levels and exhibits minimal error fluctuation, highlighting its robustness. In particular, with an accuracy solution rate comparable to PySR, ViSymRe improves the symbolic solution rate by nearly 5%, marking it the first model to achieve such a high level of symbolic solution rate. AIFeynman and PySR are competitive under noise-free conditions but show clear vulnerability as noise increases, with the symbolic solution rate and complexity showing substantial fluctuations. DSR achieves a competitive complexity comparable

to that of ViSymRe, but lags in other metrics, a problem also observed for ITEA. Overall, since the expressions in Feynman database approximate the distribution of natural laws observed in the real-world, strong performance on it indicates that ViSymRe has the potential to reveal interpretable expressions from observational or experimental data.

The ODE-Strogatz database poses a challenge to the generalization capabilities of ViSymRe, as the data points exhibit a distinct temporal order. As shown in Fig. 7b, ViSymRe maintains its leading overall ranking. Furthermore, ViSymRe demonstrates superior noise robustness compared to other models, with no significant degradation in any of its metrics under noisy scenarios; in fact, its accuracy solution rate even increases by over 10% at the noise level of 0.001 compared to that at the noise level of 0. In contrast, although PySR has a peak performance at the noise level of 0, comparable to ViSymRe, all of its metrics degrade in noisy scenarios. Other models, such as AIFeynman, AFP\_PE, and DSR, generally fall below 50% for both accuracy solution rate and symbolic solution rate, with wide confidence intervals that indicate unstable performance. Additionally, ViSymRe exhibits lower complexity than other models across all scenarios, further validating its robustness.

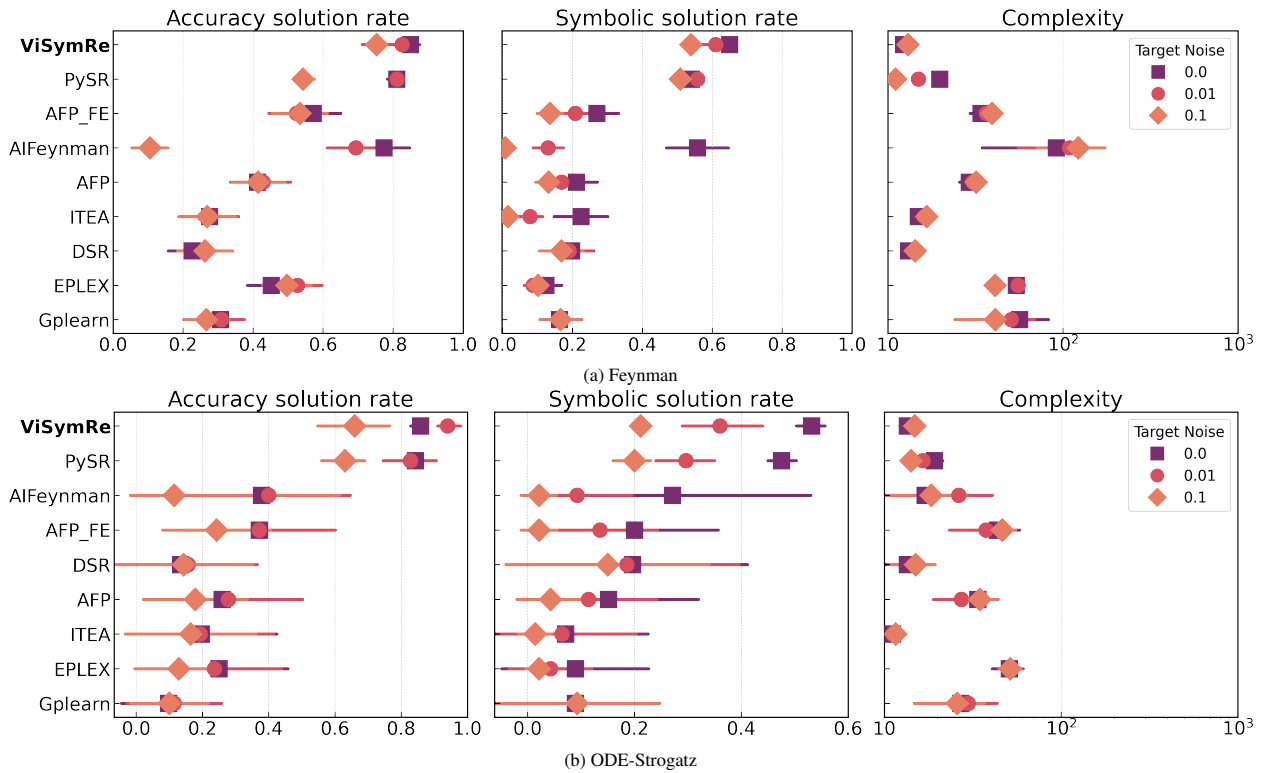


Figure 7: The results on 119 Feynman problems (top) and 14 ODE-Strogatz problems (bottom) under three levels. Models are ranked based on their overall performance. The error bars represent the 95% confidence interval.

### 5.8. Results on SRSD-Feynman benchmark

The 120 SRSD-Feynman problems are grouped in three difficulty levels: easy, medium, and hard, comprising 30, 40, and 50 problems, respectively. We compare ViSymRe and PySR on three metrics: accuracy solution rate, symbolic solution rate, and NED (see Table 2). We find that PySR performs better overall, especially in terms of accuracy solution rate and NED. However, ViSymRe shows a relative advantage in symbolic solution rate on the hard problems. The performance degradation of ViSymRe is consistent with our expectations, as the datasets used to train ViSymRe are sampled from a uniform distribution, whereas SRSD-Feynman dataset employs a log-uniform distribution with the values of the sampled points reaching up to  $10^{30}$ .

To assess the impact of distribution differences, we normalize the SRSD-Feynman dataset. The retest results show that both models improve, but ViSymRe improves more substantially. For accuracy solution rate and symbolic solution

rate, ViSymRe achieves progress on all difficulty problems and surpass PySR. For NED, ViSymRe decreases markedly, whereas PySR exhibits an upward trend (a similar trend can also be observed for symbolic solution rate on the easy problems), indicating that normalization can induce PySR to generate more complex expressions, even if this yields some improvement in the accuracy solution rate.

Table 2: Results on SRSD-Feynman (values in parentheses are on the normalized dataset).

Metric	Datasets	ViSymRe	PySR
Accuracy solution rate	Easy	63.3% ( <b>100%</b> )	66.7% ( <b>100%</b> )
	Medium	40.0% ( <b>87.5%</b> )	45.0% (85.0%)
	Hard	26.0% ( <b>76.0%</b> )	38.0% (52.0%)
Symbolic solution rate	Easy	56.6% ( <b>53.3%</b> )	60.0% (40.0%)
	Medium	27.5% ( <b>35.0%</b> )	30.0% (30.0%)
	Hard	14.0% ( <b>22.0%</b> )	4.0% (20.0%)
NED	Easy	0.611 ( <b>0.490</b> )	0.269 (0.536)
	Medium	0.735 (0.728)	0.537 ( <b>0.693</b> )
	Hard	0.884 ( <b>0.590</b> )	0.785 (0.803)

### 5.9. Alignment effectiveness analysis

To verify the effectiveness of aligning visual features with dataset features, we performed a comparative analysis of cosine similarity matrices before and after alignment. Before alignment (Fig. 8a), the similarity matrix exhibits pronounced stripe-like patterns, where specific rows or columns maintain consistently higher similarity with others, while most regions remain in the low-similarity range. This phenomenon reflects the existence of global bias between the two modalities, leading to spurious correlations. After alignment (Fig. 8b), the stripe effect disappears, and the similarity distribution becomes more uniform and block-structured. A clear diagonal band of high similarity emerges, indicating the visual and dataset features are effectively calibrated, reducing cross-modal ambiguity.

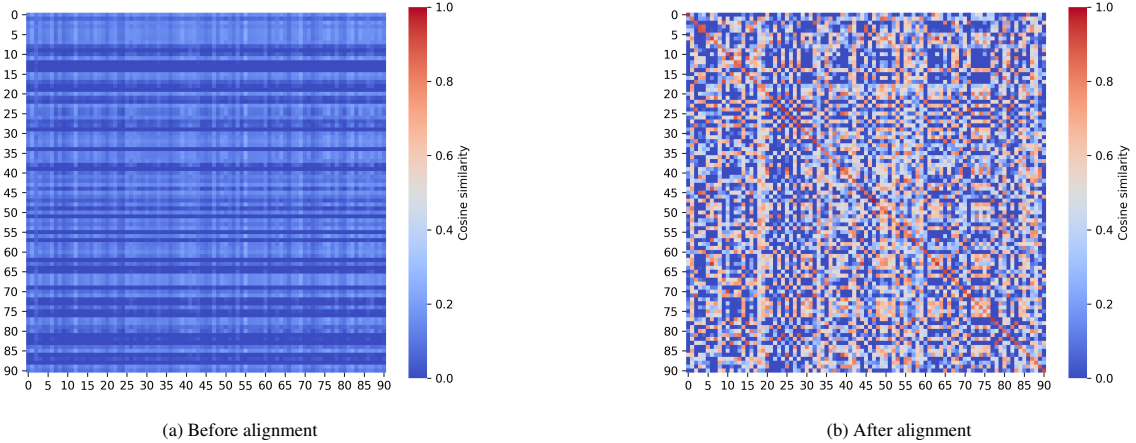


Figure 8: Cosine similarity matrices of visual and dataset features before and after alignment.

### 5.10. Ablation analysis

We conduct two types of ablations on 200 randomly generated skeletons: module ablations and factor ablations. The module ablations assess the necessity and contribution of ViSymRe’s components, including the visual modality, feature alignment, and consistency loss. To ensure fairness, ViSymRe and its variants with any module removed

are trained from scratch for 10 epochs on the same training set, which consists of 1 million skeletons with no more than three variables. The factor ablations evaluate ViSymRe’s sensitivity to key factors that affect SR performance in real-world scenarios, including the number of constants, the number of unary operators, and the number of test points. Except for the ablation factors, all other settings are fixed to the default values (three constants, three unary operators, and 200 test points). The results are shown in Fig. 9.

For the module ablations, removing the visual modality leads to the most significant performance degradation: both the accuracy solution rate and symbolic solution rate degrade by more than 10%. In contrast, removing the feature alignment or the consistency loss results in much smaller performance degradation. Across different scenarios, the accuracy solution rate and symbolic solution rate of them remain close to full ViSymRe, with the difference usually within 5%. This indicates that although the feature alignment and the consistency loss contribute positively, the visual modality remains the most crucial module for robust performance.

For the factor ablations, we observe that ViSymRe remains relatively stable when varying the number of constants and test points. But, increasing unary operators introduces greater expression complexity, which tends to reduce the symbolic solution rate and increase NED, reflecting the challenge of generating more complex expressions. However, since the ViSymRe and all its variants are trained on the expression skeletons containing at most three unary operators, we find that extending the number of unary operators from three to five does not cause noticeable performance degradation; in fact, the accuracy solution rate even improves, except for the variant without vision. Therefore, the observed performance differences are more likely to reflect the natural impact of increased task complexity rather than limitations of the model itself.

Overall, these results demonstrate that ViSymRe consistently outperforms its ablated variants, with the visual modality providing the largest performance gains. Moreover, ViSymRe also exhibits robust behavior across some key factors that affect SR performance in real-world scenarios, particularly in handling different numbers of constants and test points.

## 6. Conclusions

In recent years, the successful application of artificial intelligence (AI) for science has reignited interest in SR. As a tool for scientific modeling, SR is no longer expected to be just simple data fitting, but should also comprehensively consider efficiency as well as the simplicity and structural rationality of the generated expressions. However, existing SR models still face challenges in balancing these requirements. In this paper, we propose ViSymRe, a vision-guided multimodal pretraining SR framework that treats the expression graph as a usable resource and explores its positive role in addressing various SR challenges. Focusing on the acquisition and utilization of expression graphs, we design specialized training and inference strategies to enhance the robustness of ViSymRe in various scenarios. To enable the visualization of multivariate expressions so as to extend ViSymRe to high-dimensional scenarios, we propose a pruning method that decouples multivariate expression into independent univariate expressions, which can then be visualized as 2D curves, each representing the symbolic logic of a variable in the original expression. In addition, to address the limitation that expression graphs are unavailable during inference, we designed a dual visual processing pipeline: one is real visual encoding, which directly extracts visual features from the expression graphs available in the training phase and maps them to a finite-dimensional learnable codebook space through feature quantization; the other is virtual visual encoding, which predicts the indices of the quantized real visual features in the codebook space based on the dataset, thereby obtaining equivalent virtual visual features under graph-free conditions, breaking the reliance of traditional multimodal approaches on global resource availability.

Extensive evaluations demonstrate that ViSymRe exhibits strong robustness across various SR scenarios, achieving a leading symbolic solution rate and significantly reducing complexity, while maintaining an  $R^2$  score comparable to state-of-the-art dataset-only baselines, which highlights its potential as an effective tool for advancing scientific discovery.

**Limitations and future work** Currently, pretrained SR models remain an emerging method, though encouraging results have been achieved. A major limitation lies in generalizing these models to unseen distributions with minimal loss in performance. Although some rectification strategies based on GP and RL provide reference technical paths [28, 29, 30]. However, increasing computational time or generating “suboptimal” expression structures to obtain better data fitting results may be costly.

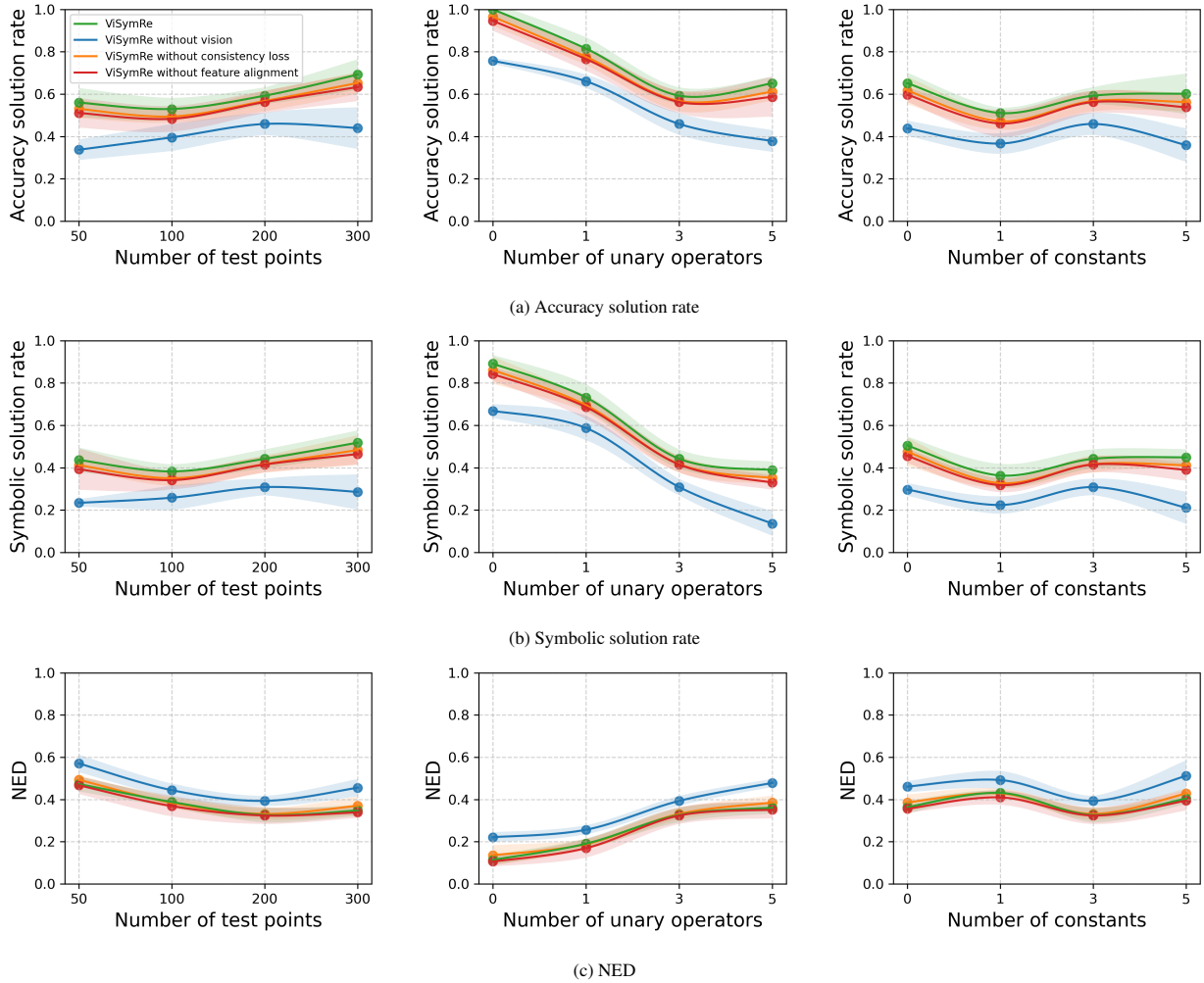


Figure 9: Ablation analysis results of ViSymRe, including the contribution of the visual modality, contrastive learning loss, and consistency loss, as well as sensitivity to the number of constants, unary operators, and test points. Each curve shows the average results of 10 independent runs, with shaded regions indicating the standard deviation.

Overall, future work for us will build on ViSymRe to explore more optimal combinations of pretrained models with GP or RL, aiming to develop a general model that is computationally efficient and capable of generating well-fitted, simple, and structurally reasonable expressions.

## Acknowledgments

This work was partially supported by Major Program of National Natural Science Foundation of China (Nos.12292980, 12292984, 12031016, 12201024), National Key R&D Program of China (Nos.2023YFA1009000, 2023YFA1009004, 2020YFA0712203, 2020YFA0712201) and Beijing Natural Science Foundation (BNSF-Z210003).

## References

- [1] M. Schmidt, H. Lipson, Distilling free-form natural laws from experimental data, *science* 324 (5923) (2009) 81–85.
- [2] H. Wang, T. Fu, Y. Du, W. Gao, K. Huang, Z. Liu, P. Chandak, S. Liu, P. Van Katwyk, A. Deac, et al., Scientific discovery in the age of artificial intelligence, *Nature* 620 (7972) (2023) 47–60.
- [3] M. Krenn, R. Pollice, S. Y. Guo, M. Aldeghi, A. Cervera-Lierta, P. Friederich, G. dos Passos Gomes, F. Häse, A. Jinich, A. Nigam, et al., On scientific understanding with artificial intelligence, *Nature Reviews Physics* 4 (12) (2022) 761–769.
- [4] M. Quade, M. Abel, K. Shafi, R. K. Niven, B. R. Noack, Prediction of dynamical systems by symbolic regression, *Physical Review E* 94 (1) (2016) 012214.
- [5] P. Neumann, L. Cao, D. Russo, V. S. Vassiliadis, A. A. Lapkin, A new formulation for symbolic regression to identify physico-chemical laws from experimental data, *Chemical Engineering Journal* 387 (2020) 123412.
- [6] S. Kim, P. Y. Lu, S. Mukherjee, M. Gilbert, L. Jing, V. Čeperić, M. Soljačić, Integration of neural network-based symbolic regression in deep learning for scientific discovery, *IEEE transactions on neural networks and learning systems* 32 (9) (2020) 4166–4177.
- [7] B. Burlacu, M. Kommenda, G. Kronberger, S. M. Winkler, M. Affenzeller, Symbolic regression in materials science: Discovering interatomic potentials from data, in: *Genetic Programming Theory and Practice XIX*, Springer, 2023, pp. 1–30.
- [8] J. R. Koza, *Genetic programming II: automatic discovery of reusable programs*, MIT press, 1994.
- [9] M. D. Schmidt, H. Lipson, Age-fitness pareto optimization, in: *Proceedings of the 12th annual conference on Genetic and evolutionary computation*, 2010, pp. 543–544.
- [10] W. La Cava, L. Spector, K. Danai, Epsilon-lexicase selection for regression, in: *Proceedings of the Genetic and Evolutionary Computation Conference 2016*, 2016, pp. 741–748.
- [11] W. La Cava, T. R. Singh, J. Taggart, S. Suri, J. H. Moore, Learning concise representations for regression by evolving networks of trees, *arXiv preprint arXiv:1807.00981* (2018).
- [12] S.-M. Udrescu, A. Tan, J. Feng, O. Neto, T. Wu, M. Tegmark, Ai feynman 2.0: Pareto-optimal symbolic regression exploiting graph modularity, *Advances in Neural Information Processing Systems* 33 (2020) 4860–4871.
- [13] E. Derner, J. Kubalik, R. Babuška, Data-driven construction of symbolic process models for reinforcement learning, in: *2018 IEEE International Conference on Robotics and Automation (ICRA)*, IEEE, 2018, pp. 5105–5112.
- [14] B. K. Petersen, M. Landajuela, T. N. Mundhenk, C. P. Santiago, S. K. Kim, J. T. Kim, Deep symbolic regression: Recovering mathematical expressions from data via risk-seeking policy gradients, *arXiv preprint arXiv:1912.04871* (2019).
- [15] T. N. Mundhenk, M. Landajuela, R. Glatt, C. P. Santiago, D. M. Faissol, B. K. Petersen, Symbolic regression via neural-guided genetic programming population seeding, *arXiv preprint arXiv:2111.00053* (2021).
- [16] P. Scholl, K. Bieker, H. Hauger, G. Kutyniok, Parfam–(neural guided) symbolic regression via continuous global optimization, in: *The Thirteenth International Conference on Learning Representations*.
- [17] L. Biggio, T. Bendinelli, A. Neitz, A. Lucchi, G. Parascandolo, Neural symbolic regression that scales, in: *International Conference on Machine Learning*, Pmlr, 2021, pp. 936–945.
- [18] M. Valipour, B. You, M. Panju, A. Ghodsi, Symbolicgpt: A generative transformer model for symbolic regression, *arXiv preprint arXiv:2106.14131* (2021).
- [19] P.-A. Kamienny, S. d’Ascoli, G. Lample, F. Charton, End-to-end symbolic regression with transformers, *Advances in Neural Information Processing Systems* 35 (2022) 10269–10281.
- [20] M. Vastl, J. Kulhánek, J. Kubalik, E. Derner, R. Babuška, Symformer: End-to-end symbolic regression using transformer-based architecture, *IEEE Access* (2024).
- [21] Y. Li, J. Liu, M. Wu, L. Yu, W. Li, X. Ning, W. Li, M. Hao, Y. Deng, S. Wei, Mmsr: Symbolic regression is a multi-modal information fusion task, *Information Fusion* 114 (2025) 102681.
- [22] R. Zhang, P. Isola, A. A. Efros, Colorful image colorization, in: *Computer Vision–ECCV 2016: 14th European Conference, Amsterdam, The Netherlands, October 11–14, 2016, Proceedings, Part III* 14, Springer, 2016, pp. 649–666.
- [23] P. Esser, R. Rombach, B. Ommer, Taming transformers for high-resolution image synthesis, in: *Proceedings of the IEEE/CVF conference on computer vision and pattern recognition*, 2021, pp. 12873–12883.
- [24] I. Arnaldo, K. Krawiec, U.-M. O’Reilly, Multiple regression genetic programming, in: *Proceedings of the 2014 Annual Conference on Genetic and Evolutionary Computation*, 2014, pp. 879–886.
- [25] M. Virgolin, T. Alderliesten, P. A. Bosman, Linear scaling with and within semantic backpropagation-based genetic programming for symbolic regression, in: *Proceedings of the genetic and evolutionary computation conference*, 2019, pp. 1084–1092.
- [26] M. Cramer, Interpretable machine learning for science with pysr and symbolicregression.jl, *arXiv preprint arXiv:2305.01582* (2023).
- [27] G. Martius, C. H. Lampert, Extrapolation and learning equations, *arXiv preprint arXiv:1610.02995* (2016).

- [28] M. Landajuela, C. S. Lee, J. Yang, R. Glatt, C. P. Santiago, I. Aravena, T. Mundhenk, G. Mulcahy, B. K. Petersen, A unified framework for deep symbolic regression, *Advances in Neural Information Processing Systems* 35 (2022) 33985–33998.
- [29] P. Shojaei, K. Meidani, A. Barati Farimani, C. Reddy, Transformer-based planning for symbolic regression, *Advances in Neural Information Processing Systems* 36 (2023) 45907–45919.
- [30] J. Liu, W. Li, L. Yu, M. Wu, L. Sun, W. Li, Y. Li, Snr: Symbolic network-based rectifiable learning framework for symbolic regression, *Neural Networks* 165 (2023) 1021–1034.
- [31] S. Holt, Z. Qian, M. van der Schaar, Deep generative symbolic regression, *arXiv preprint arXiv:2401.00282* (2023).
- [32] Y. Li, W. Li, L. Yu, M. Wu, J. Liu, W. Li, M. Hao, S. Wei, Y. Deng, Discovering mathematical formulas from data via gpt-guided monte carlo tree search, *arXiv preprint arXiv:2401.14424* (2024).
- [33] J. Ngiam, A. Khosla, M. Kim, J. Nam, H. Lee, A. Y. Ng, Multimodal deep learning, in: *Proceedings of the 28th international conference on machine learning (ICML-11)*, 2011, pp. 689–696.
- [34] N. Srivastava, R. R. Salakhutdinov, Multimodal learning with deep boltzmann machines, *Advances in neural information processing systems* 25 (2012).
- [35] A. Fukui, D. H. Park, D. Yang, A. Rohrbach, T. Darrell, M. Rohrbach, Multimodal compact bilinear pooling for visual question answering and visual grounding, *arXiv preprint arXiv:1606.01847* (2016).
- [36] A. Radford, J. W. Kim, C. Hallacy, A. Ramesh, G. Goh, S. Agarwal, G. Sastry, A. Askell, P. Mishkin, J. Clark, et al., Learning transferable visual models from natural language supervision, in: *International conference on machine learning*, PMLR, 2021, pp. 8748–8763.
- [37] J. Li, R. Selvaraju, A. Gotmare, S. Joty, C. Xiong, S. C. H. Hoi, Align before fuse: Vision and language representation learning with momentum distillation, *Advances in neural information processing systems* 34 (2021) 9694–9705.
- [38] C. Jia, Y. Yang, Y. Xia, Y.-T. Chen, Z. Parekh, H. Pham, Q. Le, Y.-H. Sung, Z. Li, T. Duerig, Scaling up visual and vision-language representation learning with noisy text supervision, in: *International conference on machine learning*, PMLR, 2021, pp. 4904–4916.
- [39] J. Lu, D. Batra, D. Parikh, S. Lee, Vilbert: Pretraining task-agnostic visiolinguistic representations for vision-and-language tasks, *Advances in neural information processing systems* 32 (2019).
- [40] H. Tan, M. Bansal, Lxmert: Learning cross-modality encoder representations from transformers, *arXiv preprint arXiv:1908.07490* (2019).
- [41] A. Ramesh, M. Pavlov, G. Goh, S. Gray, C. Voss, A. Radford, M. Chen, I. Sutskever, Zero-shot text-to-image generation, in: *International conference on machine learning*, Pmlr, 2021, pp. 8821–8831.
- [42] C. Saharia, W. Chan, S. Saxena, L. Li, J. Whang, E. L. Denton, K. Ghasemipour, R. Gontijo Lopes, B. Karagol Ayan, T. Salimans, et al., Photorealistic text-to-image diffusion models with deep language understanding, *Advances in neural information processing systems* 35 (2022) 36479–36494.
- [43] Z. Liu, Y. Wang, S. Vaidya, F. Ruehle, J. Halverson, M. Soljačić, T. Y. Hou, M. Tegmark, Kan: Kolmogorov-arnold networks, *arXiv preprint arXiv:2404.19756* (2024).
- [44] M. Ding, Z. Yang, W. Hong, W. Zheng, C. Zhou, D. Yin, J. Lin, X. Zou, Z. Shao, H. Yang, et al., Cogview: Mastering text-to-image generation via transformers, *Advances in neural information processing systems* 34 (2021) 19822–19835.
- [45] E. Jang, S. Gu, B. Poole, Categorical reparameterization with gumbel-softmax, *arXiv preprint arXiv:1611.01144* (2016).
- [46] N. Q. Uy, N. X. Hoai, M. O’Neill, R. I. McKay, E. Galván-López, Semantically-based crossover in genetic programming: application to real-valued symbolic regression, *Genetic Programming and Evolvable Machines* 12 (2011) 91–119.
- [47] M. Keijzer, Improving symbolic regression with interval arithmetic and linear scaling, in: *European Conference on Genetic Programming*, Springer, 2003, pp. 70–82.
- [48] M. F. Korn, Accuracy in symbolic regression, *Genetic Programming Theory and Practice IX* (2011) 129–151.
- [49] Y. Jin, W. Fu, J. Kang, J. Guo, J. Guo, Bayesian symbolic regression, *arXiv preprint arXiv:1910.08892* (2019).
- [50] W. La Cava, P. Orzechowski, B. Burlacu, F. O. de França, M. Virgolin, Y. Jin, M. Kommenda, J. H. Moore, Contemporary symbolic regression methods and their relative performance, *arXiv preprint arXiv:2107.14351* (2021).
- [51] R. P. Feynman, R. B. Leighton, M. Sands, *The Feynman lectures on physics, Vol. I: The new millennium edition: mainly mechanics, radiation, and heat*, Vol. 1, Basic books, 2015.
- [52] S. H. Strogatz, *Nonlinear dynamics and chaos: with applications to physics, biology, chemistry, and engineering*, CRC press, 2018.
- [53] Y. Matsubara, N. Chiba, R. Igarashi, Y. Ushiku, Rethinking symbolic regression datasets and benchmarks for scientific discovery, *arXiv preprint arXiv:2206.10540* (2022).
- [54] F. O. de Franca, G. S. I. Aldeia, Interaction–transformation evolutionary algorithm for symbolic regression, *Evolutionary computation* 29 (3) (2021) 367–390.

## Appendix A. Data generation

### Appendix A.1. Expression skeleton generator

The method we employ for generating expression skeletons is improved from the open-source provided by [17]. In this approach, expression is conceptualized as a binary tree. The non-leaf nodes represent operators. The leaf nodes are reserved for the variables or constants. In Table A.3, we present the comprehensive parameters employed by our expression skeleton generator. Note that although the distribution of exponents and constants is pre-defined, they produce a wider distribution after internal operations, such as  $(x^3)^3 \rightarrow x^9$ . In addition, we restrict physically invalid operator couplings, as described in Section 4.3.2, to prevent the generation of poor quality expression skeletons.

Table A.3: The parameters employed by expression generator.

Description	Value
Max number of variables	10
Max number of unary operators	5
Max number of binary operators	$Number(variables) + 5$
Max number of constants	5
Max number of nodes	50
Distribute of constants	$\mathcal{U}(0, 10)$
Frequency of binary operators	add:1, sub:0.5, mul:1, div:0.5
Frequency of unary operators	abs:0.1, pow2:1, pow3:1, pow5:0.1, sqrt:0.5, sin:0.5, cos:0.5, tan:0.1, arcsin:0.1, log:0.1, exp:0.5

### Appendix A.2. Data points sampling

For each expression skeleton, we first sample constants following the distribution in Table A.3, and then sample  $n$  points for each variable. To enhance the diversity of sample distributions, we divide  $n$  points into  $k$  clusters, where  $k$  follows a discrete uniform distribution  $\mathcal{U}\{1, \dots, 5\}$ . The points of each cluster are independently sampled from  $\mathcal{U}(-\alpha, \alpha)$ . Here,  $\alpha$  follows a discrete uniform distribution  $\mathcal{U}\{1, \dots, 10\}$ . Once the constants and variables are sampled, we substitute them into the expression skeleton to compute the target, thereby generating the complete dataset  $D = \{X_i, y_i\}_{i=1}^n \in \mathbb{R}^{n \times (d+1)}$  as input for training ViSymRe. If any extreme values (such as NaN or Inf) are detected in the target, both the target and its corresponding variable values are set to zero.

## Appendix B. Main parameters

The main parameters of ViSymRe are shown in Table B.4.

## Appendix C. IEEE-754

The IEEE-754 standard is a binary representation method used in computer science. It represents floating-point numbers in the following form:

$$(-1)^S \times 1.F \times 2^{(E-\text{bias})}$$

where  $S$  is the sign bit (0 for positive, 1 for negative),  $E$  is the biased exponent,  $F$  is the fractional part, and bias is a fixed offset added to the actual exponent to represent both positive and negative exponents (bias = 127 for single precision). For example, in the 32-bit single-precision format, the structure consists of 1 bit for the sign, 8 bits for the exponent, and 23 bits for the fraction. In certain applications, reduced-precision formats (e.g., with an 8-bit fraction) are used for better performance.

Table B.4: The default parameters employed of ViSymRe.

<b>Description</b>	<b>Symbol</b>	<b>Value</b>
<b>Architecture</b>		
Number of dataset encoder layers	~	4
Number of virtual visual encoder layers	~	2
Number of feature fusion layers	~	2
Number of Transformer decoder layers	~	12
Number of real visual encoder layers	~	4
Model dimension	~	512
<b>Pre-training</b>		
Optimizer	~	Adam
Learning rate	~	0.0001-0.00001
Learning rate decay	~	Cosine annealing
Batch size	~	300
Number of sampled data points	n	200
Number of (real or virtual) visual features	m	64
Number of vectors in codebook space	K	512
<b>Testing</b>		
Beam size	C	10-30
Number of bags	B	10
Number of test points per bag	~	200
Initial sampling range of constant for BFGS	~	$\mathcal{U}(0, 10)$
Number of BFGS restarts	~	10